Applied Surface Science 721 (2026) 165458

Contents lists available at ScienceDirect

Applied Surface Science

journal homepage: www.elsevier.com/locate/apsusc

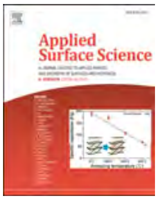

Full Length Article

Co_3O_4-FeOOH as a heterojunction electrocatalyst for highly-efficient hydrazine-assisted water electrolysis and pollutant degradation

Liyuan Dai [a], Yuta Tsuji [b], Hiroki Iwai [a], Quan Quan [c], Dongyuan Song [a], Xueda Liu [a], Jiangyang Liu [d], Takeshi Yanagida [d], Johnny C. Ho [c,e,f,*], SenPo Yip [e,**]

[a] Interdisciplinary Graduate School of Engineering Sciences, Kyushu University, Fukuoka 816-8580, Japan
[b] Faculty of Engineering Sciences, Kyushu University, Fukuoka 816-8580, Japan
[c] Department of Materials Science and Engineering, City University of Hong Kong, Hong Kong SAR 999077, PR China
[d] Department of Applied Chemistry, Graduate School of Engineering, The University of Tokyo, Tokyo 113-8656, Japan
[e] Institute for Materials Chemical and Engineering, Kyushu University, Fukuoka 816-8580, Japan
[f] State Key Laboratory of Terahertz and Millimeter Waves, City University of Hong Kong, Hong Kong SAR 999077, PR China

ARTICLE INFO

Keywords:
Electrocatalyst
Heterojunction
Water electrolysis
Pollutant degradation

ABSTRACT

The hydrazine oxidation reaction (HzOR) offers a promising alternative to mitigate the high energy demands associated with the kinetically sluggish oxygen evolution reaction. Consequently, developing an efficient electrocatalyst for HzOR is crucial. In this study, we present a highly effective Co_3O_4-FeOOH heterojunction designed to enhance hydrazine-assisted water splitting performance. Various characterization techniques were employed to analyze the structures and compositions of the catalyst. Evaluations of its electrocatalytic performance revealed exceptional catalytic activity during hydrazine electrolysis, achieving a current density of 100 mA cm^{-2} with a minimal negative potential of −17.2 mV (vs. RHE). The system exhibited impressive stability, maintaining consistent performance for over 100 h during HzOR. Notably, the heterostructure electrocatalyst demonstrated outstanding performance and stability in simulated seawater, requiring only −70 mV (vs.RHE) to deliver a current density of 100 mA cm^{-2} and remaining stable after the durability test. The electrocatalyst also performed well in harsh environments, including brine and highly alkaline environments. These findings highlight the potential of the Co_3O_4-FeOOH heterostructure electrocatalyst for energy-efficient hydrogen production and pollutant degradation.

1. Introduction

The excessive consumption of fossil fuels has led to the emission of massive amounts of greenhouse gases into the atmosphere, contributing to climate change and widespread environmental pollution [1–3]. There is an urgent need for clean, emission-free, and sustainable energy sources as alternatives [4–7]. Hydrogen stands out as an ideal candidate for renewable energy due to its high energy density and emission-free nature during consumption [8–15].

In recent years, electrochemical water splitting has emerged as a promising strategy among various hydrogen production methods [16,17]. This process involves two half-reactions: the hydrogen evolution reaction (HER) at the cathode and the oxygen evolution reaction (OER) at the anode [18]. Compared to HER, OER is a four-electron transfer process that is kinetically sluggish and requires a high theoretical electrode potential (1.23 V vs RHE), significantly reducing overall conversion efficiency and increasing power consumption, making the water electrolysis process energy-intensive and less favorable from a sustainability standpoint [19–21]. Therefore, anodic electrochemical reactions with lower electrode potentials, such as the oxidation of small molecules like hydrazine, urea, alcohols, sulfones, amines, glucose, and aldehydes, are being explored to replace the energy-intensive OER [8,22].

Among these reactions, the hydrazine oxidation reaction (HzOR, $N_2H_4 + 4OH^- \rightarrow N_2 + 4H_2O + 4e^-$) is extensively studied due to its significantly lower theoretical electrode potential (−0.33 V vs. RHE), which helps mitigate the drawbacks associated with the OER [23,24]. Hydrazine is widely used as a raw chemical in various fields, including

---

* Corresponding author at: Department of Materials Science and Engineering, City University of Hong Kong, Hong Kong SAR 999077, PR China.
** Corresponding author.

E-mail addresses: johnnyho@cityu.edu.hk (J.C. Ho), yip.sen.po.472@m.kyushu-u.ac.jp (S. Yip).

https://doi.org/10.1016/j.apsusc.2025.165458
Received 11 September 2025; Received in revised form 20 November 2025; Accepted 1 December 2025

industry, agriculture, medicine, and dye synthesis [25–27]. However, its extensive application can have adverse effects on environment, ecological balance, agricultural productivity, and may even pose serious risk to human health if not properly managed [28,29]. Once it enters the human body, hydrazine can rapidly induce symptoms such as dizziness, nausea, cough and dyspnea. It can also corrode the skin, causing redness, pain, and even ulceration [27]. The HzOR can serve as a dual purpose by neutralizing hydrazine-containing industrial waste while enabling energy-saving hydrogen production, making it an effective strategy for both pollutant degradation and sustainable energy generation [30]. Therefore, coupling pollutant degradation with hydrogen production is a highly forward-looking endeavour [27,31]. In this context, developing highly efficient electrocatalysts for HzOR is crucial.

Currently, the development of electrocatalysts based on earth-abundant elements (such as Fe, Ni, and Co), including transition metal oxides (TMOs), hydroxides, phosphides, and selenides, is receiving significant attention as a cost-effective strategy for sustainable catalysis [32–35]. TMOs, in particular, have emerged as promising electrocatalysts for anodic electrochemical reactions such as the OER and HzOR, owing to their low cost, earth abundance, and good stability in alkaline media [36–39]. The diverse chemical states of TMOs facilitate efficient charge transfer, crucial for enhancing HzOR performance. Among various TMOs, Co-based oxides like Co_3O_4 and their heterostructures have demonstrated good activity due to mixed valence states of Co species (Co^{2+} and Co^{3+}), which enhance electron transport and increase the number of active sites [40–42]. High valence cations exhibit strong intrinsic activity toward HzOR, contributing to reduced overpotential and enhanced reaction kinetics [27,42,43]. Moreover, strong interfacial interactions in heterostructures can accelerate charge transfer and optimize the adsorption/desorption behaviors of reaction intermediates, attributed to the electronic coupling between different components [44–48]. Heterostructure engineering is therefore regarded as one of the most promising strategies for improving anodic reaction performance in hydrolysis [49]. Moreover, the hierarchical porous structure of heterostructures offers abundant channels for electrolyte penetration and gas diffusion, thereby facilitating mass transfer [50,51].

In this study, we fabricated a porous Co_3O_4-FeOOH heterojunction on conductive nickel foam (NF), combining the strong adsorption capability of Fe-based oxide/hydroxides for electrocatalytic intermediates with the robust HzOR activity of Co_3O_4 [52]. The resulting electrocatalyst exhibited remarkable activity towards HzOR, achieving a low potential of −17.2 mV (vs. RHE) at a current density of 100 mA cm^{-2} and requiring only 122.1 mV (vs. RHE) to reach 400 mA cm^{-2}. The outstanding bifunctional electrocatalytic performance of Co_3O_4-FeOOH heterojunction enables efficient overall hydrazine splitting (OHzS). In a two-electrode configuration, a cell voltage of only 0.49 V was required to deliver a current density of 300 mA cm^{-2}. The electrocatalyst demonstrates remarkable stability, maintaining continuous operation for over 116 h at 100 mA cm^{-2} in HzOR. The excellent performance of the electrocatalyst can also extends to harsh conditions such as simulated seawater, highly saline environments, and strong alkaline media. More importantly, the electrocatalyst exhibited high degradation efficiency for hydrazine-containing solutions, highlighting its potential for both clean hydrogen production and pollutant elimination.

2. Methodology

2.1. Materials and chemicals

Cobalt nitrate hexahydrate ($Co(NO_3)_2{\cdot}6H_2O$, 99.9 %) was purchased from Kojundo Chemical Laboratory Co., Ltd. (Japan). Ethanol (EtOH, C_2H_6O, 99.5 %), acetone (C_3H_6O, 99.5 %), ferrous chloride tetrahydrate ($FeCl_2{\cdot}4H_2O$, 99.0 %), urea ($CO(NH_2)_2$, 90 %), potassium hydroxide (KOH, 85 %), sodium chloride (NaCl, 90 %), para-dimethylaminobenzaldehyde (PDAB, $C_9H_{11}NO$) and hydrochloric acid (HCl, 30 %) were purchased from FUJIFILM Wako Pure Chemical Co. (Japan). Hydrazine monohydrate ($N_2H_4{\cdot}H_2O$, 98 %) was purchased from Sigma-Aldrich, Ltd. NF was purchased from Goodfellow, Ltd. All reagents used in this study were used without further purification.

2.2. Preparation of Co_3O_4-FeOOH

The Co_3O_4-FeOOH heterostructure electrocatalyst was prepared via a three-step process, as shown in Fig. 1. Firstly, before the synthesis, a piece of NF was cleaned in 1.0 M HCl, acetone, and ethanol subsequently. Then, FeOOH layer was prepared by immersing the cleaned NF in a 50 mM $FeCl_2$ solution and putting it into a microwave oven at 900 W for one minute. The product was washed with deionized water and ethanol, and dried overnight at 60 ℃ in a vacuum oven. Co_3O_4-FeOOH was synthesized according to the previous report [53]. In brief, 1.455 g of $Co(NO_3)_2$ and 1.818 g of urea were dissolved in a mixture containing deionized water and ethyl alcohol in a glass bottle (volume ratio, 1:1, 100 mL) under ultrasonication. After drying, the FeOOH-coated NF was placed in the above solution, sealed with a cap, and heated at 90 ℃ for 8 h in a furnace. The Co_3O_4-FeOOH was obtained by calcining the dried intermediate at 400 ℃ for 2 h in a muffle furnace.

2.3. Characterizations

X-ray diffractometer (XRD, Rigaku SmartLab), with Cu Ka radiation source (1.5418 Å), was employed to investigate the phases and crystal structures of the electrocatalysts. Scanning electron microscopy (SEM, Thermo Fisher Scientific Helios Hydra CX), with a working voltage of 10 kV, was used to examine the morphologies, and the energy-dispersive spectrometry (EDS, Oxford instruments Xplore) was used to investigate the composition. A transmission electron microscope (TEM, Thermo Fisher Talos F200X) was used to further investigate the morphologies and microstructures. X-ray photoelectron spectroscopy (XPS, Shimadzu/KRATOS Corporation AXIS-165) was applied to investigate the surface chemical properties of the samples. The ultraviolet photoelectron spectroscopy (UPS, Thermo Scientific Nexsa, Avantage v.59921) was employed to determine the work function (W_f) of the samples, using a He I excitation source ($h\nu = 21.2$ eV). A −5 V bias was applied to the samples during the UPS measurement. The value of W_f was calculated using the photoelectric equation, $W_f = h\nu - W$.

2.4. Theoretical computation

The crystal structures of Co_3O_4 and γ-FeOOH, obtained from the ICDD Powder Diffraction File (PDF 43-1003 for Co_3O_4; PDF 73-2326 for γ-FeOOH), were fully optimized within density functional theory (DFT) as implemented in the Vienna ab initio simulation package (VASP) [54–56]. The Perdew–Burke–Ernzerhof (PBE) functional [57] was used with a plane-wave basis set and the projector-augmented wave (PAW) method [58]. The on-site Coulomb interaction was treated within the DFT + U framework using Dudarev's approach [59]. For Fe 3d states, U = 7.0 eV and J = 1.0 eV were applied following a previous report [60], while no U correction was applied to the Co 3d states, also in accordance with a prior study [61]. Antiferromagnetic initial spin configurations were assigned for both Co_3O_4 and γ-FeOOH based on these previous reports. The plane-wave cutoff energy was set to 500 eV. The convergence criterion for the electronic self-consistent field (SCF) loop was set to 1.0×10^{-5} eV. Both the atomic positions and cell parameters were fully optimized until the forces on all the atoms became less than 0.03 eV/Å. The Γ-centered k-point meshes with a k spacing of $2\pi \times 0.05$ $Å^{-1}$ were employed for sampling the Brillouin zone. Grimme's D3 dispersion correction formalism with Becke–Johnson damping (D3BJ) [62,63] was adopted. Optimized structures shown in this paper were drawn by using VESTA [64]. Slab models of the Co_3O_4 (440) and γ-FeOOH (020) surfaces were generated from the optimized bulk structures using the method developed by Hinuma et al. [65–67]. Each slab was constructed with a thickness of approximately 8 Å and a vacuum layer of about 15 Å

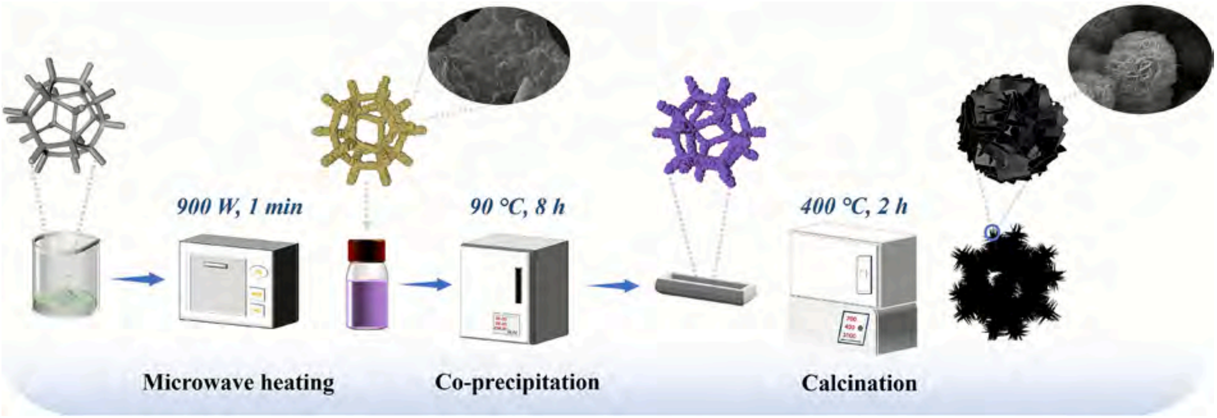

Fig. 1. Schematic illustration of the synthesis of Co_3O_4-FeOOH on NF.

to avoid spurious interactions between periodic images. Among the possible lattice-matching configurations generated using the Interface Builder in QuantumATK, the Co_3O_4 (440)/γ-FeOOH (020) interface with a mean absolute strain of 0.96 % was selected. To explore possible atomic arrangements at the interface, one of the slabs was laterally translated parallel to the interface plane, generating twelve distinct Co_3O_4 (440)/γ-FeOOH (020) interface configurations. To obtain the most stable interfacial configuration, all twelve Co_3O_4 (440)/γ-FeOOH (020) interface models were optimized using the Preferred Potential (PFP) version v7.0.0, a universal Neural Network Potential (NNP) provided by Matlantis Inc [68,69]. The optimization was performed using the Limited-memory Broyden–Fletcher–Goldfarb–Shanno (LBFGS) method [70] with a convergence threshold of 1.0×10^{-4} eV/Å, applying the ExpCellFilter to allow full relaxation of both atomic positions and the cell parameters. The CRYSTAL_PLUS_D3 mode was adopted to include dispersion effects via the D3BJ correction. With the Becke–Johnson damping function. The most stable interface structure obtained from the NNP calculations was further optimized using VASP. The computational parameters were identical to those employed for the individual bulk structure optimizations described above. For the optimized interface structure, the charge density difference and Bader charge analyses [71–74] were performed to investigate the charge redistribution and interfacial charge transfer characteristics.

2.5. Electrochemical measurements

The electrocatalytic performance was evaluated using the conventional three-electrode system. A carbon rod and a saturated calomel electrode were employed as the counter and reference electrodes, respectively. The electrolyte was 0.5 M N_2H_4 + 1 M KOH for HzOR, while 1 M KOH was used for the OER. All the electrochemical tests were carried out using an electrochemical workstation (Gamry 1010E, USA). The linear sweep voltammetry (LSV) curves were obtained with a scanning rate of 10 mV s^{-1}, and were calibrated with iR compensation in the electrochemical workstation. The electrochemical impedance spectroscopy (EIS) was performed at 100 mV throughout a frequency range of 100 kHz to 0.01 Hz. All the potentials obtained were converted to the potentials vs. reversible hydrogen electrode (RHE) using the Nernst equation:

$$E_{RHE} = E_{Hg/HgO} - 0.059 \times pH + E^{\theta}{}_{Hg/HgO} \tag{1}$$

where $E^{\theta}{}_{Hg/HgO}$ is 98 mV. The Tafel relationship was derived from the LSV curve, and the simplified Butler-Volmer formula was applied to represent it:

$$\eta = a + b \times log|j| \tag{2}$$

where η represents overpotential, $a = -b \times logj_0$, j_0 is exchange current density, j is current density, and b represents Tafel slope.

2.6. Hydrazine degradation behavior examination

The hydrazine degradation rate was estimated via spectrophotometry [30]. During hydrazine electrolysis, 1 mL of electrolyte was extracted every 20 min to measure the absorbance of N_2H_4, using an ultraviolet–visible spectrophotometer at 458 nm. Under acidic conditions, N_2H_4 reacts with PDAB to form a stable-colored complex, enabling the concentration of N_2H_4 to be determined indirectly by measuring the absorbance of the complex. The acidic condition was created by adding 0.12 M of HCl to the extracted electrolyte. The concentration of N_2H_4 at a certain interval was determined from the obtained calibration curve, shown in Fig. S1.

3. Results and discussion

To confirm the successful synthesis of the heterostructure, the crystal structure of the samples was studied by XRD. The XRD patterns in Fig. 2a show that FeOOH was successfully synthesized on NF (JSPDS No. 73-2326), and Co_3O_4 was synthesized on the γ-FeOOH layer (JSPDS No. 43-1003). The diffraction peaks observed at 2θ = 14.64°, 26.71°, 35.20°, and 41.31°correspond to the (0 2 0), (0 2 1), (1 3 0), and (1 1 1) facets of γ-FeOOH, respectively, while the weak signal intensities indicate its low crystallinity [75]. No obvious diffraction peaks originating from other impurity phases, such as FeO, Fe_2O_3, and Fe_3O_4, were observed, indicating the successful preparation of phase-pure FeOOH product by the microwave treatment. The diffraction peaks located at 19.0°, 31.27°, 36.84°, 43.31°, 54.24°, 59.02° and 65.23° can be assigned to (1 1 1), (2 2 0), (3 1 1), (2 2 2), (4 2 2), (5 1 1) and (4 4 0) lattice planes of Co_3O_4, respectively. The as-prepared Co_3O_4 was identified as a cubic spinel phase with space group Fd3m, which shows fine crystallization [76,77]. The results match well with the observation by TEM-Selected area electron diffraction (SAED, discuss later).

The morphologies of the samples were observed by SEM. In Fig. 2b, the FeOOH sample shows a rough surface, indicating that the iron oxide-hydroxide layer was grown on the NF during the microwave treatment. After Co_3O_4 deposition, globe-flower-shaped particles, with an average size of about 6 μm, were observed (Fig. 2c). The flower-like particles, composed of interconnected nanosheets, significantly increase the specific surface area. This unique structure provides abundant adsorption sites, which enhance N_2H_4 interaction, promote the activation and adsorption of intermediates, and improve mass transport efficiency during electrochemical processes. The contact angle (CA) measurement further demonstrates that the growth of Co_3O_4 on the FeOOH layer enhances the surface hydrophilicity. As shown in Fig. S2, the Co_3O_4-FeOOH exhibits a CA of 0 degrees, indicating complete wettability. In contrast, pure FeOOH shows a CA of 89.7 degrees, reflecting its

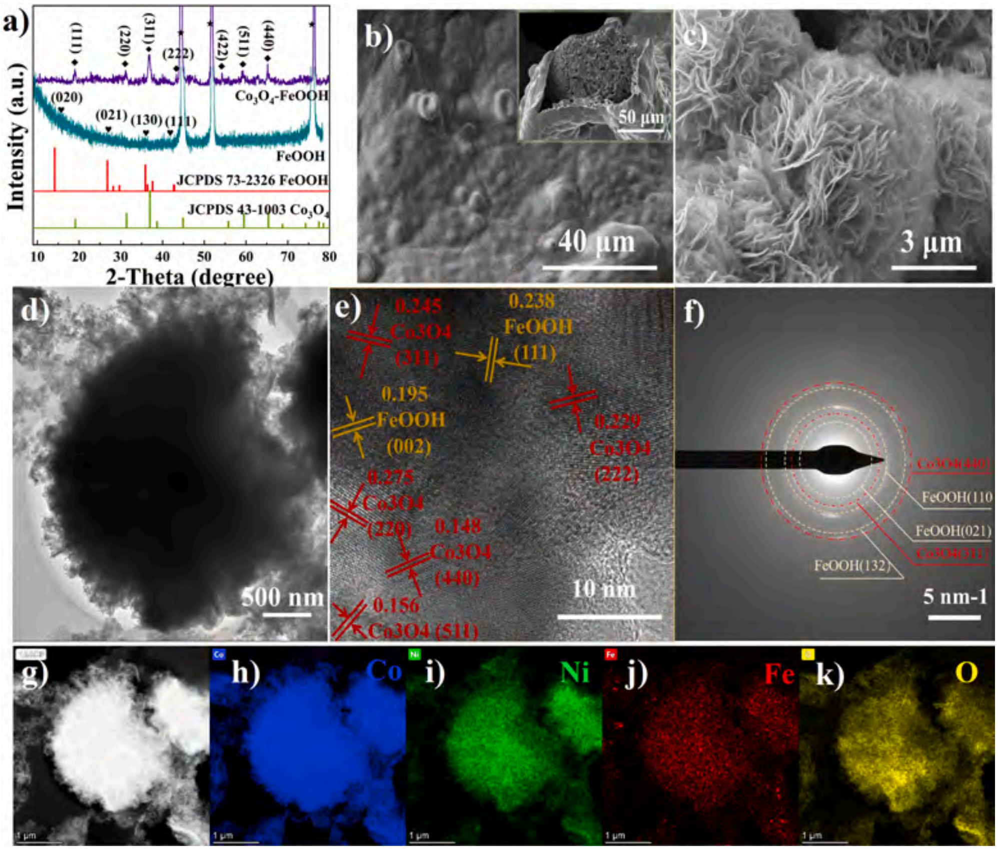

Fig. 2. a) XRD patterns of various samples; b) SEM images of FeOOH layer, and c) Co_3O_4-FeOOH; d) TEM image, e) HRTEM image, f) SAED pattern, g) HAADF image, and h)-k) the corresponding element distribution of Co_3O_4-FeOOH.

relatively poor hydrophilicity. Pure Co_3O_4 also displays a CA of 0 degrees, suggesting that the excellent hydrophilicity of the heterostructure primarily originates from the surface morphology and microstructure contributed by the surface Co_3O_4 layer.

TEM image (Fig. 2d) shows that the morphology of Co_3O_4-FeOOH matches well with the SEM observation. The high-resolution transmission electron microscopy (HRTEM) image in Fig. 2e exhibits the multiple interfaces of FeOOH and Co_3O_4. The clear lattice fringes with spacing of 0.245 nm, 0.229 nm, 0.275 nm, 0.156 nm, and 0.148 nm are found and can be assigned to (3 1 1), (2 2 2), (2 2 0), (5 1 1), and (4 4 0) planes of Co_3O_4. Another set of well-defined lattice fringes with interplanar distances of 0.238 nm and 0.159 nm can be ascribed to the (1 1 1) and (0 0 2) planes of FeOOH. The co-existence of two phases confirmed the heterostructure formation, which is further confirmed by the SAED patterns displayed in Fig. 2f. The diffraction rings associated with the (4 4 0), and (3 1 1) planes of Co_3O_4, and (1 1 0), (0 2 1), and (1 3 2) planes of FeOOH were observed. The multiple rings assembled with bright spots in the SAED pattern also demonstrated the polycrystalline nature of the sample. High-angle annular dark-field scanning transmission electron microscopy (HAADF-STEM) image and the corresponding elements distribution mappings (Fig. 2g–k) represent the distribution of Fe, Co, Ni, and O on the electrocatalyst surface, implying the successful formation of Co_3O_4-FeOOH/NF heterojunction catalyst.

XPS analysis was conducted to examine the surface chemical environment of the heterojunction electrocatalyst. The full-survey XPS spectrum displayed in Fig. S3 indicates the existence of Co, Fe, O, and Ni in the electrocatalyst. The O 1s spectrum can be deconvoluted into three peaks, located at 529.2, 531.8, and 533.1 eV, which can correspond to the lattice oxygen, oxygen vacancy, and adsorbed oxygen, respectively, as shown in Fig. 3a. The existence of the oxygen vacancies on the catalyst surface enhances the electrocatalytic reaction activity [78]. As shown in the Ni 2p core level XPS spectrum in Fig. 3b, the Ni $2p_{3/2}$ and the Ni $2p_{1/2}$ peaks, together with their corresponding satellite features associated with Ni^{2+} species, indicate the oxidation state of Ni on the surface. However, the weak peak intensities indicate that only a minor amount of Ni exists in the samples. In Fe 2p spectra, the peaks at 709.58 and 729.3 eV ($\Delta BE = 18.9$ eV) can be ascribed to Fe $2p_{3/2}$ and Fe $2p_{1/2}$ [79]. Deconvoluted peaks at 710.5, 722.5, 711.68, and 726.02 eV, correspond to the $2p_{3/2}$, and the $2p_{1/2}$ of Fe^{2+} and the $2p_{3/2}$, the $2p_{1/2}$ of Fe^{3+} in Co_3O_4-FeOOH, and the peaks at 710.48, 723.7, 714.3, and 726.08 eV, corresponding to the $2p_{3/2}$, and the $2p_{1/2}$ of Fe^{2+}, and the $2p_{3/2}$, and the $2p_{1/2}$ of Fe^{3+} in FeOOH, showing a negative shift in binding energy after Co_3O_4 deposition, as shown in Fig. 3c [80,81]. In the high-resolution Co 2p XPS spectrum (Fig. 3d), the peaks located at 776.3 and 792.5 eV ($\Delta BE = 16.2$ eV) are associated with the Co $2p_{3/2}$ and the Co $2p_{1/2}$, respectively. The peaks at 775.1 and 791.0 eV can be assigned to the $2p_{3/2}$ and the $2p_{1/2}$ of Co^{3+}, while the peaks at 777.68 and 793.38 eV can be assigned to the $2p_{3/2}$ and the $2p_{1/2}$ of Co^{2+} [82]. In contrast to pristine FeOOH, the Fe 2p peaks in Co_3O_4–FeOOH shift to lower binding energies, indicating a redistribution of electron density between Co_3O_4 and FeOOH, owing to the difference in Fermi levels. This suggests successfully formation of an electronically coupled interface between FeOOH and Co_3O_4 [28,83]. By comparing the calculated Co^{3+}/Co^{2+} ratios of pure Co_3O_4 (Fig. S4) and Co_3O_4-FeOOH, the heterojunction exhibits a slightly higher ratio than the pure material, further supporting the presence of charge transfer between Co_3O_4 and FeOOH, within the heterojunction. This interfacial charge redistribution promotes electronic structure modulation and accelerates the reaction kinetics.

UPS was employed to investigate the electronic properties of the heterojunction [84]. The calculated W_f of Co_3O_4, and Co_3O_4-FeOOH are 4.33 eV, and 4.29 eV, respectively. The decrease in W_f after Co_3O_4 comes

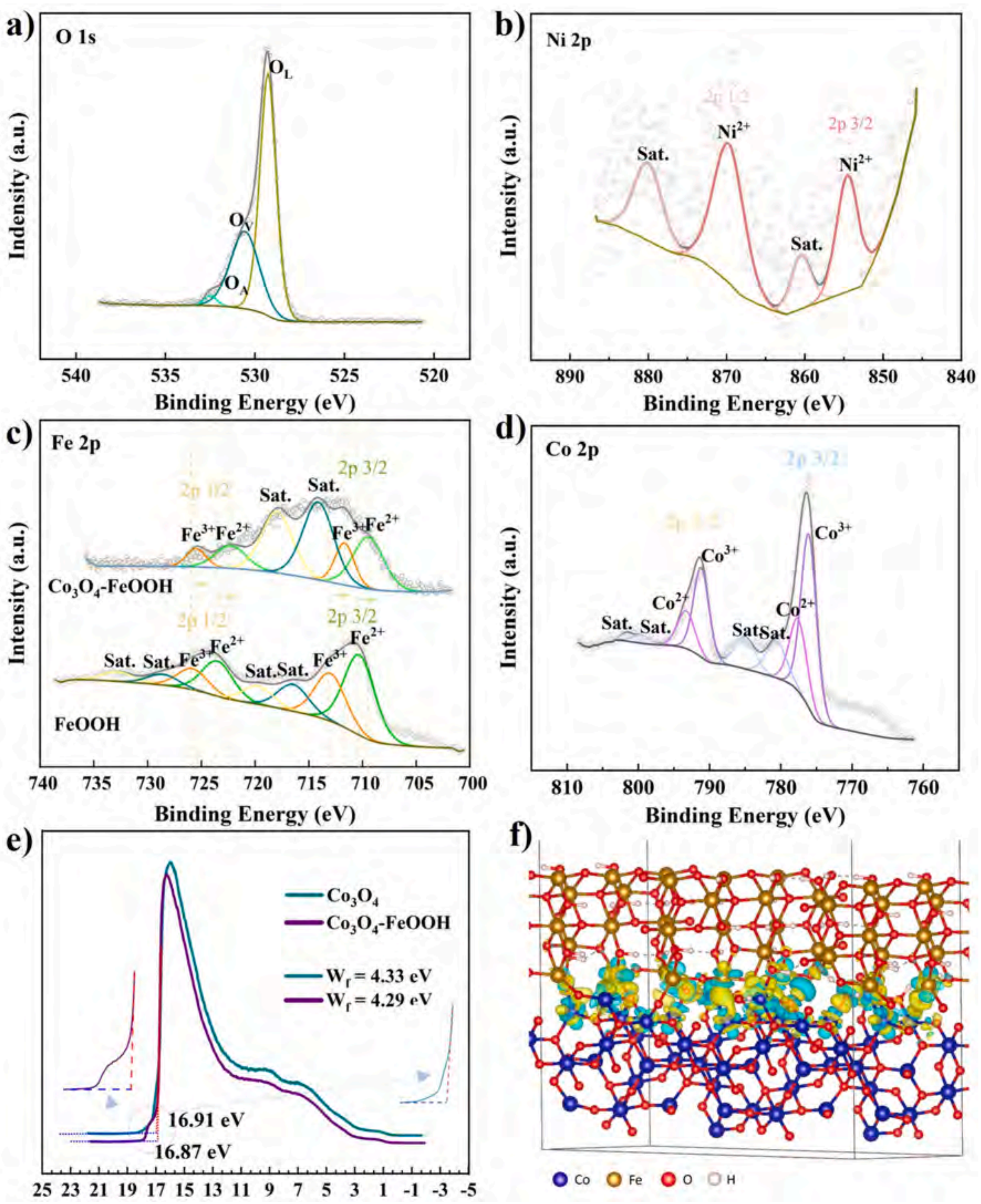

Fig. 3. Core level spectra of a) O 1s; b) Ni 2p, c) Fe 2p, and d) Co 2p of Co_3O_4-FeOOH; e) UPS spectrum of Co_3O_4, and Co_3O_4-FeOOH; f) Charge-density difference (0.005 bohr^{-3} isosurface; yellow = charge accumulation, blue = charge depletion) for the Co_3O_4 (440)/γ-FeOOH(020) interface.

into contact with the FeOOH layer indicates interfacial electron transfer between Co_3O_4 and FeOOH, as shown in Fig. 3e. Theoretical calculation also verified the formation of this interfacial electronic field. As shown in Fig. 3f, the charge-density difference for the optimized Co_3O_4(440)/γ-FeOOH(020) interface reveals pronounced electron redistribution concentrated at the Fe–O–Co linkages and at interfacial H bonds formed between Fe–OH and Co–OH groups. These features indicate strong interfacial interactions and an electronically coupled interface, leading to a modulation of the local electronic structure. Consistently, Bader analysis yields a net charge of −0.16 |e| on the γ-FeOOH slab and +0.16 |e| on the Co_3O_4 slab, confirming charge transfer from Co_3O_4 to γ-FeOOH.

LSV was carried out to evaluate the performance of Co_3O_4-FeOOH towards HzOR and OER, shown in Fig. 4a, where the electrolyte was 0.5 M N_2H_4 + 1 M KOH in the HzOR, while being 1 M KOH in the OER. The Co_3O_4-FeOOH electrocatalyst exhibits a remarkable catalytic activity toward the HzOR, enabling low working potential in hydrazine-assisted electrolysis compared to the much higher voltages required for the OER. A small negative potential of −17.2 mV (vs. RHE) is sufficient to drive a current density of 100 mA cm^{-2}, significantly lower than that required for the OER (1.583 V, vs. RHE), indicating a substantially reduced energy input, surpassing previously reported studies (Table S1). In addition, a high current density of 400 mA cm^{-2} was delivered at 122.1 mV (vs. RHE), demonstrating the potential for substantial energy savings at

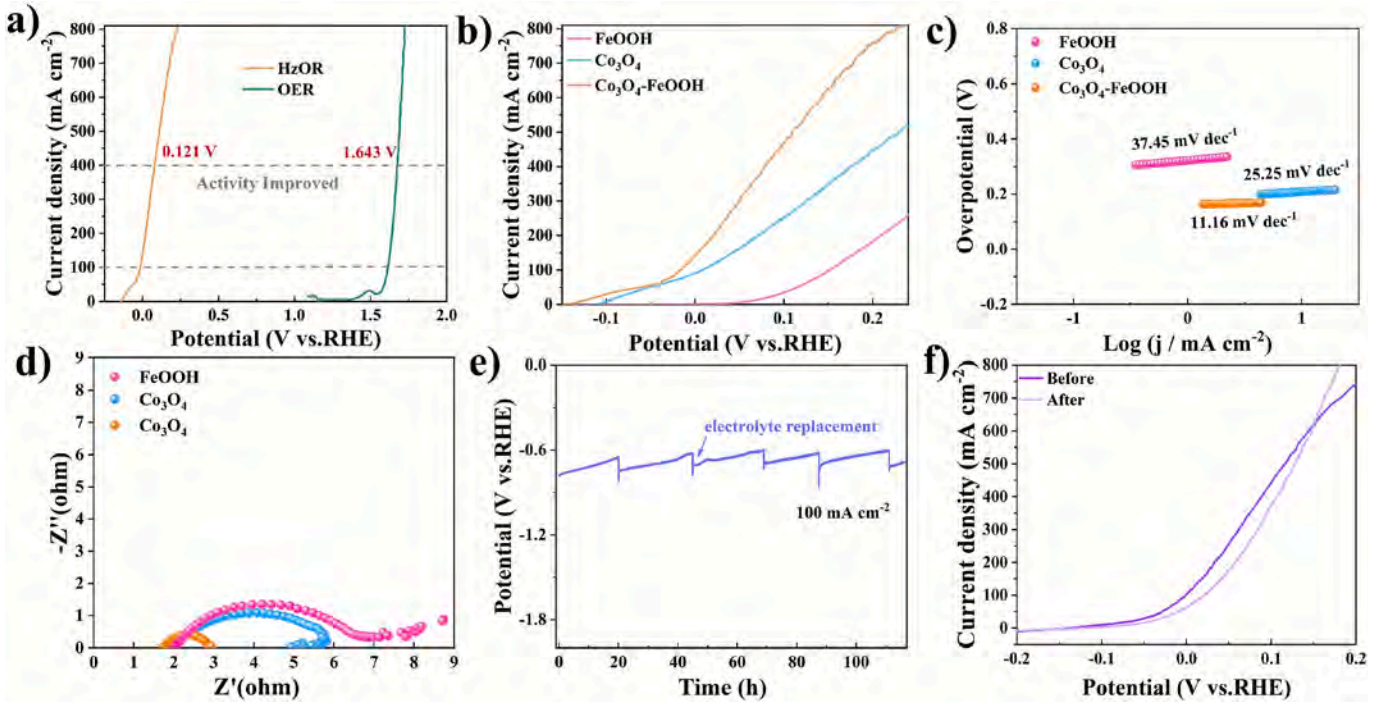

Fig. 4. a) Performances of Co$_3$O$_4$-FeOOH in HzOR (1 M KOH + 0.5 M N_2H_4) and OER (1 M KOH); b) LSV curves of Co$_3$O$_4$-FeOOH, Co$_3$O$_4$, and FeOOH during HzOR; c) Tafel slopes derives from LSVs; d) EIS curves of Co$_3$O$_4$-FeOOH, Co$_3$O$_4$, and FeOOH in HzOR; e) Stability test of Co$_3$O$_4$-FeOOH in HzOR, and f) LSV curves of Co$_3$O$_4$-FeOOH before and after stability test.

higher current density operation. To demonstrate the superior catalytic activity of Co$_3$O$_4$-FeOOH heterojunction, the HzOR performances of the constituting components, Co$_3$O$_4$ and FeOOH, were also examined under the same conditions. As shown in Fig. 4b, at a current density of 200 mA cm^{-2}, the Co$_3$O$_4$-FeOOH exhibits a notable catalytic activity with a low potential of 20 mV (vs. RHE), which is significantly lower than that of the potential of Co$_3$O$_4$ (72 mV, vs. RHE) and FeOOH (210 mV, vs. RHE). The result further indicates that the Co$_3$O$_4$ is the primary active component for the HzOR. Tafel plots were derived from the LSV polarization curves to investigate the electrochemical kinetics of the HzOR. As shown in Fig. 4c, the Tafel slope of Co$_3$O$_4$-FeOOH (11.16 mV dec^{-1}) is much smaller than that of FeOOH (37.45 mV dec^{-1}), and slightly lower than that of Co$_3$O$_4$ (25.25 mV dec^{-1}), proving the favorable catalytic kinetics towards HzOR of the heterojunction. The reaction kinetics were further assessed by electrochemical impedance spectroscopy (EIS). From the Nyquist curves in Fig. 4d, Co$_3$O$_4$-FeOOH has a much smaller semicircle radius than that of the Co$_3$O$_4$ and FeOOH, indicating a much lower electrode-transfer-resistance (R_{ct}) and thus a higher charge-transfer rate and more rapid catalytic kinetics [85,86]. The result indicates that the electron migration is accelerated by the enhanced interaction between the Co$_3$O$_4$ and FeOOH after Co$_3$O$_4$ deposition on FeOOH, which improves the electron-transfer capacity of the catalyst [87].

The long-term stability of the heterostructure electrocatalyst was examined by chronopotentiometry (CP) test. The CP curve in Fig. 4e shows that the potential remains stable for more than 116 h at a current density of 100 mA cm^{-2}. The LSV polarization curve was measured again (Fig. 4f) after the CP test, which shows negligible attenuation. The structure and valence state changes of the catalyst after stability test were also investigated, and the results are shown in Fig. S5. SEM analysis of the post-CP-test electrocatalyst (Fig. S5a) shows some morphological transformation, with the ball-shaped particles becoming smaller. Comparing the EDS data with the pre-reaction state (Fig. S5b, Fig. S6, Table S2), no significant changes in the Fe, Co and O ratio were observed, indicating that no noticeable outward diffusion occurred. In contrast, the Co^{2+}/Co^{3+} and Fe^{2+}/Fe^{3+} ratios increased, implying that both Co^{3+} and Fe^{3+} in the Co$_3$O$_4$-FeOOH heterojunction participated in the oxidation of N_2H_4 throughout the reaction.

Cyclic voltammetry (CVs) were used to quantify the electrochemical surface area, and double layer capacitance (C_{dl}). The effective electrochemically active surface area (ECSA) can be calculated using the equation: $ECSA = C_{dl}/C_s$, where C_s is the specific capacitance. The C_{dl} value was evaluated from the CVs recorded at different scan rates (Fig. S7), and the results are shown in Fig. S8. The Co$_3$O$_4$-FeOOH sample exhibits a much larger C_{dl} (12.16 mF cm^{-2}) than that of the FeOOH (4.42 mF cm^{-2}), indicating that Co$_3$O$_4$-FeOOH possesses a higher ECSA than FeOOH. This demonstrates that the heterojunction electrocatalyst provides more accessible catalytic sites and achieves higher atomic utilization efficiency towards HzOR.

The HER activities of Co$_3$O$_4$-FeOOH, Co$_3$O$_4$, and FeOOH were also evaluated in the electrolyte, which consisted of 1 M KOH and 0.5 M N_2H_4. As shown in Fig. 5a, Co$_3$O$_4$-FeOOH requires a potential of −358 mV (vs. RHE) to deliver a current density of −200 mA cm^{-2}, while Co$_3$O$_4$ and FeOOH require −402 mV (vs. RHE) and −398 mV (vs. RHE) to deliver the same current density, respectively. The HER performance of the heterojunction catalyst is better than that of its constituent components. The Tafel slopes of Co$_3$O$_4$-FeOOH (94.92 mV dec^{-1}), Co$_3$O$_4$ (123.3 mV dec^{-1}), and FeOOH (150.3 mV dec^{-1}) were obtained from the corresponding LSV curves. The results implies that the H_2 production in our electrochemical system depending on the Volmer step ($H_2O + e^- \rightarrow H_{ad} + OH^-$). The smaller Tafel slope of Co$_3$O$_4$-FeOOH compared with the other two samples indicates faster hydrogen adsorption on the heterojunction surface [88,89], confirming the accelerated HER kinetic of Co$_3$O$_4$-FeOOH (Fig. 5b). The EIS curves shown in Fig. 5c proves the faster charge transfer of Co$_3$O$_4$-FeOOH among all the samples prepared. These results suggest that the hetero-interface between Co$_3$O$_4$ and FeOOH also plays a crucial role in hydrogen evolution. The durability test displayed in Fig. 5d demonstrates the good stability of the electrocatalyst towards the HER, with a well-maintained potential over 22 h, and shows almost no change in performance, as shown from LSV curves after the stability test (Fig. 5e), which illustrates the favorable HER activity of Co$_3$O$_4$-FeOOH.

Due to the excellent HzOR and HER performance, a two-electrode

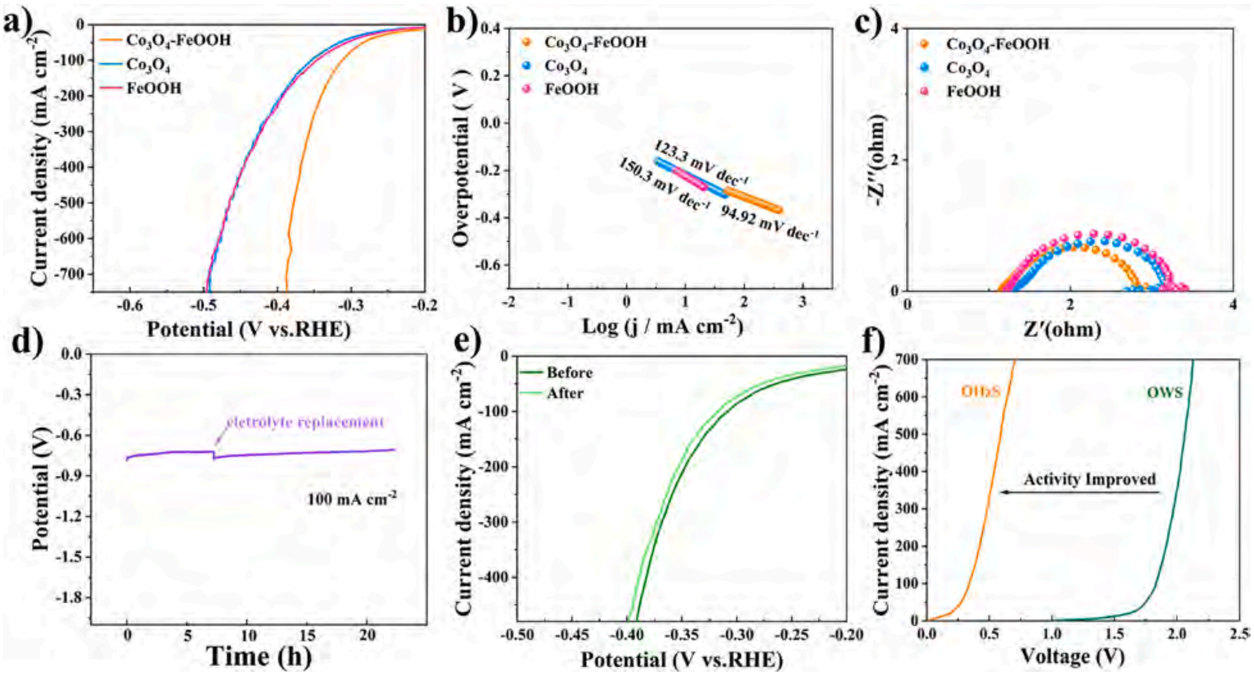

Fig. 5. a) Performances of Co_3O_4-FeOOH, Co_3O_4, and FeOOH in HER; b) Tafel slopes extracted from a); c) EIS curves of Co_3O_4-FeOOH, Co_3O_4, and FeOOH in HER; d) CP test of Co_3O_4-FeOOH in HER, and e) LSV curves of Co_3O_4-FeOOH before and after stability test; f) Performances of Co_3O_4-FeOOH in OHzS (1 M KOH + 0.5 M N_2H_4), and OWS (1 M KOH).

cell was constructed to examine the electrocatalytic H_2 production ability, with Co_3O_4-FeOOH being both anode and cathode. The LSV curves of overall water splitting (OWS) and overall hydrazine splitting (OHzS) were measured, as shown in Fig. 5f. A significant energy saving performance in OHzS was obtained, where only 0.49 V is required to deliver a current density of 300 mA cm^{-2}. In comparison, 1.95 V is required in OWS to achieve the same current density.

Hydrazine is a water pollutant that is highly toxic, carcinogenic, and poses serious health and environmental hazards. Therefore, achieving a high degradation rate in wastewater treatment is of great importance [90]. Coupling hydrogen production and hydrazine degradation can realize the ideal combination of high-efficiency hydrogen production and pollutant degradation with low energy consumption. Here, the Watt and Crisp method was employed to evaluate the N_2H_4 degradation rate [91]. In short, equal volume of electrolyte was collected during the HzOR at a current density of 100 mA^{-2}. The residual hydrazine concentration was determined from the absorbance of the developed color, and the degradation rate was subsequently estimated. The results showed that 100 mg / L of hydrazine was almost completely degraded after 20 min (Fig. 6), with a degradation rate of nearly 100 %, demonstrating a fast degradation rate and high efficiency. At the same time, the kinetics of the N_2H_4 degradation process were investigated, as shown in Fig. S9. The high R^2 value (0.9999) indicates the best fit, suggesting that the degradation of N_2H_4 in this electrocatalytic system follows the BMG (Behnajady–Modirshahla–Ghanbery) kinetic model [92]. The result proves that it is possible to realize high hydrogen output and efficient hydrazine degradation with low energy consumption.

Given the excellent electrocatalytic performance of the Co_3O_4-FeOOH electrocatalyst, it is potentially applicable in various scenarios, such as seawater-coupled hydrogen production and other harsh environments, including highly alkaline solutions and alkaline brines. For hydrazine electrolysis, whether in simulated seawater (0.5 M NaCl + 1.0 M KOH), alkaline brine (2.5 M NaCl + 1.0 M KOH), or strong alkaline solution (2.5 M KOH), Co_3O_4–FeOOH exhibits remarkable electrocatalytic performance, as shown in Fig. 7, Figs. S10 and S11. Interestingly, the catalytic activity improves with increasing NaCl

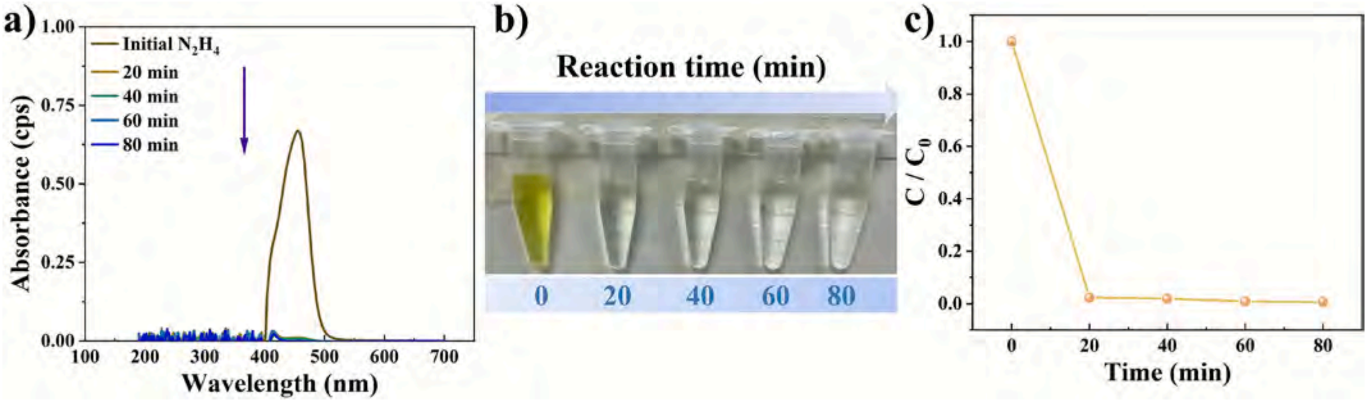

Fig. 6. a) Evolution of UV–Vis absorption peak in OHZS; b) color change of the complex at different reaction times in the system; c) Hydrazine degradation rate in OHzS.

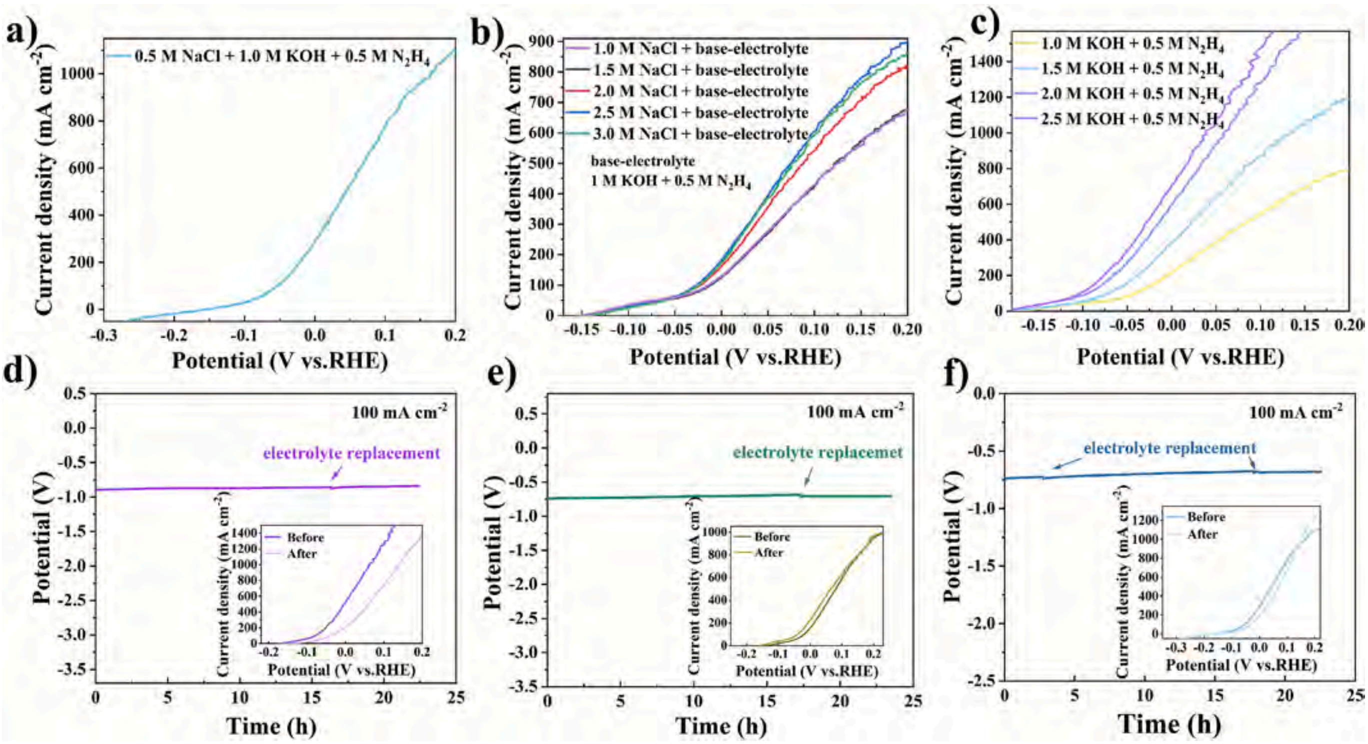

Fig. 7. LSV curves of Co_3O_4-FeOOH during HzOR in different system: a) simulated seawater; b) 1.0 M KOH + NaCl (1.0 M−3.0 M) + 0.5 M N_2H_4; and c) KOH (1.0 M−2.5 M) + 0.5 M N_2H_4. CP curves and corresponding LSVs of Co_3O_4-FeOOH before and after the stability test in different systems: d) simulated seawater; e) 1.0 M KOH + NaCl (2.5 M) + 0.5 M N_2H_4; and f) KOH (2.5 M) + 0.5 M N_2H_4.

concentration, probably due to enhanced solution conductivity. However, beyond a certain salt concentration (2.5 M NaCl), the performance enhancement was saturated. Similarly, increasing the KOH concentration also improves electrocatalytic performance, probably for a similar reason. Long-term stability tests in hydrazine-containing highly salty electrolytes (2.5 M NaCl + 0.5 M N_2H_4 + 1 M KOH) and highly alkaline electrolytes (2.5 M KOH + 0.5 M N_2H_4) confirm the catalyst's outstanding durability and electrochemical kinetics under high-salt and strong alkali conditions. Overall, the results demonstrate that the Co_3O_4-FeOOH electrocatalyst holds great promise for energy-saving hydrogen production and pollution treatment.

4. Conclusion

In summary, a Co_3O_4-FeOOH heterojunction electrocatalyst was successfully developed, significantly enhancing the electrocatalytic performance of the HzOR through the built-in electric field. Remarkably low potentials of −17.2 mV (vs. RHE) and 122.1 mV (vs.RHE) are required to achieve current densities of 100 and 400 mA cm^{-2}, respectively, which are substantially lower than those needed for the OER to reach the same current densities. The HER performance of Co_3O_4-FeOOH has also shown improvement compared to the individual components. Furthermore, the catalyst's high activity facilitates energy-efficient hydrogen production in HzOR-coupled water electrolysis, achieving an impressively low potential of 0.49 V at a current density of 300 mA cm^{-2} in OHzS. In comparison, conventional OWS demands a much higher potential of 1.95 V to reach the same current density, demonstrating significant energy savings. Beyond its excellent electrocatalytic performance in HzOR, the catalyst exhibits outstanding stability and activity under harsh conditions, such as simulated seawater, highly alkaline environments, and high-salinity media, highlighting its great potential in hydrogen production and pollutant treatment.

CRediT authorship contribution statement

Liyuan Dai: Writing – original draft, Software, Methodology, Investigation, Formal analysis, Data curation. **Yuta Tsuji:** Software, Writing – review & editing, Validation. **Hiroki Iwai:** Software, Validation, Writing – review & editing. **Quan Quan:** Validation, Writing – review & editing, Formal analysis. **Dongyuan Song:** Investigation, Data curation. **Xueda Liu:** Validation, Investigation. **Jiangyang Liu:** Investigation, Methodology, Writing – review & editing, Formal analysis. **Takeshi Yanagida:** Writing – review & editing, Supervision, Conceptualization. **Johnny C. Ho:** Writing – review & editing, Supervision, Resources, Methodology, Formal analysis, Conceptualization. **SenPo Yip:** Writing – review & editing, Resources, Methodology, Formal analysis, Conceptualization.

Declaration of competing interest

The authors declare that they have no known competing financial interests or personal relationships that could have appeared to influence the work reported in this paper.

Acknowledgments

We thank Dr. Kohei Kusada and Mr. Daiki Takahashi for helpful discussions. This work was funded by "Network Joint Research Center for Materials and Devices" of the Ministry of Education, Culture, Sports, Science and Technology (MEXT). The first author acknowledges the support of the China Scholarship Council (CSC) program. YT acknowledges support from JSPS KAKENHI (JP25K00065) and from JSPS Grants-in-Aid for Transformative Research Areas (A)—"Supra-ceramics" (JP22H05146) and "Machine Learning Physics" (JP25H01541). The computations in this work were performed using the computer facilities at the Research Institute for Information Technology, Kyushu University, at the Supercomputer Center, Institute for Solid State Physics, University of Tokyo, and at the Cyberscience Center, Tohoku University. This work was also supported through the activities of VDEC, d.lab, The University of Tokyo, in collaboration with NIHON SYNOPSYS G.K.

Appendix A. Supplementary data

Supplementary data to this article can be found online at https://doi.org/10.1016/j.apsusc.2025.165458.

Data availability

Data will be made available on request.

References

[1] J. Wang, W. Azam, Natural resource scarcity, fossil fuel energy consumption, and total greenhouse gas emissions in top emitting countries, Geosci. Front. 15 (2) (2024) 101757.

[2] T. Martins, A.C. Barreto, F.M. Souza, A.M. Souza, Fossil fuels consumption and carbon dioxide emissions in G7 countries: empirical evidence from ARDL bounds testing approach, Environ. Pollut. 291 (2021) 118093.

[3] F. Perera, Pollution from fossil-fuel combustion is the leading environmental threat to global pediatric health and equity: solutions exist, Int. J. Environ. Res. Public Health 15 (1) (2017) 16.

[4] P.J. Megía, A.J. Vizcaíno, J.A. Calles, A. Carrero, Hydrogen production technologies: from fossil fuels toward renewable sources. A mini review, Energy Fuels 35 (20) (2021) 16403–16415.

[5] H. Sun, X. Xu, L. Fei, W. Zhou, Z. Shao, Electrochemical oxidation of small molecules for energy-saving hydrogen production, Angew. Chem. Int. Ed. 14 (30) (2024) 2401242.

[6] Y. Zhai, C. Jin, Q. Xia, W. Han, J. Wu, X. Zhao, X. Zhang, Atomically confined Ru sites in octahedral Co_3O_4 for high-efficiency hydrazine oxidation, Adv. Funct. Mater. 34 (13) (2023) 2311063.

[7] Q. Zhang, W. Zhang, J. Zhu, X. Zhou, G.R. Xu, D. Chen, Z. Wu, L. Wang, Tuning d–p orbital hybridization of $NiMoO_4$@$Mo_{15}Se_{19}$/$NiSe_2$ core-shell nanomaterials via asymmetric coordination interaction enables the water oxidation process, Adv. Energy Mater. 14 (20) (2024) 2304546.

[8] T. Wang, X. Cao, L. Jiao, Progress in hydrogen production coupled with electrochemical oxidation of small molecules, Angew. Chem. Int. Ed. 61 (50) (2022) e202213328.

[9] C. Tang, R. Zhang, W. Lu, Z. Wang, D. Liu, S. Hao, G. Du, A.M. Asiri, X. Sun, Energy-saving electrolytic hydrogen generation: Ni_2P nanoarray as a high-performance non-noble-metal electrocatalyst, Angew. Chem. Int. Ed. Engl. 56 (3) (2017) 842–846.

[10] N. Armaroli, V. Balzani, The hydrogen issue, ChemSusChem 4 (2011) 21–36.

[11] Q. Hu, G. Li, G. Li, X. Liu, B. Zhu, X. Chai, Q. Zhang, J. Liu, C. He, Trifunctional electrocatalysis on dual-doped graphene nanorings integrated boxes for efficient water splitting and Zn–air batteries, Adv. Energy Mater. 9 (14) (2019) 1803867.

[12] W. Wang, M. Xu, X. Xu, W. Zhou, Z. Shao, Perovskite oxide based electrodes for high-performance photoelectrochemical water splitting, Angew. Chem. Int. Ed. 59 (2019) 136–152.

[13] Y. Gong, Y. Zhi, Y. Lin, T. Zhou, J. Li, F. Jiao, W. Wang, Controlled synthesis of bifunctional particle-like Mo/Mn-NixSy/NF electrocatalyst for highly efficient overall water splitting, Dalton Trans. 48 (20) (2019) 6718–6729.

[14] Y. Yan, T. He, B. Zhao, K. Qi, H. Liu, B.Y. Xia, Metal/covalent–organic frameworks-based electrocatalysts for water splitting, J. Mater. Chem. A 6 (33) (2018) 15905–15926.

[15] A. Raveendran, M. Chandran, R. Dhanusuraman, A comprehensive review on the electrochemical parameters and recent material development of electrochemical water splitting electrocatalysts, RSC Adv. 13 (6) (2023) 3843–3876.

[16] J.E. Lee, K.-J. Jeon, P.L. Show, I.H. Lee, S.-C. Jung, Y.J. Choi, G.H. Rhee, K.-Y.-A. Lin, Y.-K. Park, Mini review on H_2 production from electrochemical water splitting according to special nanostructured morphology of electrocatalysts, Fuel 308 (2022) 122048.

[17] Q. Qian, Y. Zhu, N. Ahmad, Y. Feng, H. Zhang, M. Cheng, H. Liu, C. Xiao, G. Zhang, Y. Xie, Recent advancements in electrochemical hydrogen production via hybrid water splitting, Adv. Mater. 36 (4) (2023) 2306108.

[18] S.C. Cho, J.H. Seok, H.N. Manh, J.H. Seol, C.H. Lee, S.U. Lee, Expanding the frontiers of electrocatalysis: advanced theoretical methods for water splitting, Nano Convergence 12 (1) (2025) 4.

[19] P. Aghamohammadi, B. Hüner, O.C. Altıncı, E.T. Akgul, B. Teymur, U.B. Simsek, M. Demir, Recent advances in the electrocatalytic applications (HER, OER, ORR, water splitting) of transition metal borides (MBenes) materials, Int. J. Hydrogen Energy 87 (2024) 179–198.

[20] S.M.A. Nayem, S. Islam, M.A. Aziz, A.J.S. Ahammad, Mechanistic insight into hydrothermally prepared molybdenum-based electrocatalyst for overall water splitting, Electrochim. Acta 445 (2023) 142050.

[21] G. Lee, S.E. Jun, Y. Kim, I.-H. Park, H.W. Jang, S.H. Park, K.C. Kwon, Multicomponent metal oxide- and metal hydroxide-based electrocatalysts for alkaline water splitting, Materials 16 (8) (2023) 3280.

[22] L. Zeng, Y. Chen, M. Sun, Q. Huang, K. Sun, J. Ma, J. Li, H. Tan, M. Li, Y. Pan, Y. Liu, M. Luo, B. Huang, S. Guo, Cooperative Rh-O5/Ni(Fe) site for efficient biomass upgrading coupled with H_2 production, J. Am. Chem. Soc. 145 (32) (2023) 17577–17587.

[23] T.Y. Burshtein, Y. Yasman, L. Muñoz-Moene, J.H. Zagal, D. Eisenberg, Hydrazine oxidation electrocatalysis, ACS Catal. 14 (4) (2024) 2264–2283.

[24] H.-Y. Wang, Z.-Y. Yuan, Hydrazine-assisted water electrolysis system: performance enhancement and application expansion, Mater. Horiz. 12 (14) (2025) 5123–5148.

[25] U. Ragnarsson, Synthetic methodology for alkyl substituted hydrazines, Chem. Soc. Rev. 30 (2001) 205–213.

[26] K. Siddharth, P. Alam, M.D. Hossain, N. Xie, G.S. Nambafu, F. Rehman, J.W. Y. Lam, G. Chen, J. Cheng, Z. Luo, G. Chen, B.Z. Tang, M. Shao, Hydrazine detection during ammonia electro-oxidation using an aggregation-induced emission dye, J. Am. Chem. Soc. 143 (5) (2021) 2433–2440.

[27] J. Li, H. Duan, Recent progress in energy-saving hydrogen production by coupling with value-added anodic reactions, Chem 10 (10) (2024) 3008–3039.

[28] D. Xiong, X. He, X. Liu, S. Gong, C. Xu, Z. Tu, D. Wu, J. Wang, Z. Chen, 1D/3D heterogeneous assembling body of cobalt nitrides for highly efficient overall hydrazine splitting and supercapacitors, Small 20 (8) (2023) e2306100.

[29] X. Xu, H.-C. Chen, L. Li, M. Humayun, X. Zhang, H. Sun, D. Debecker, W. Zhang, L. Dai, C. Wang, Leveraging metal nodes in metal-organic frameworks for advanced anodic hydrazine oxidation assisted seawater splitting, ACS Nano 17 (11) (2023) 10906–10917.

[30] J. Chi, L. Guo, J. Mao, T. Cui, J. Zhu, Y. Xia, J. Lai, L. Wang, Modulation of electron structure and dehydrogenation kinetics of nickel phosphide for hydrazine-assisted self-powered hydrogen production in seawater, Adv. Funct. Mater. 33 (46) (2023) 2300625.

[31] Y. Zhou, T. Tian, S. Jiang, R. Shen, H. Yu, Z. Wang, H. Wang, L. Wang, K. Deng, Alternating pulse driven periodic reactivation of high-entropy mesoporous film boosts continuous membrane-free PET waste upcycling coupled with H_2 production, Adv. Funct. Mater. (2025) e11835.

[32] Q. Sun, Y. Li, J. Wang, B. Cao, Y. Yu, C. Zhou, G. Zhang, Z. Wang, C. Zhao, Pulsed electrodeposition of well-ordered nanoporous Cu-doped Ni arrays promotes high-efficiency overall hydrazine splitting, J. Mater. Chem. A 8 (40) (2020) 21084–21093.

[33] R. Guo, Y. Zhang, X. Zhang, M. Ma, T. Hu, Enhanced catalytic oxidation of hydrazine of CoO/Co_3O_4 heterojunction on N-doped carbon, Electrochim. Acta 458 (2023) 142537.

[34] F. Song, W. Li, J. Yang, G. Han, P. Liao, Y. Sun, Interfacing nickel nitride and nickel boosts both electrocatalytic hydrogen evolution and oxidation reactions, Nat. Commun. 9 (2018) 4531.

[35] F. Yang, X. Bao, P. Li, X. Wang, G. Cheng, S. Chen, W. Luo, Boosting hydrogen oxidation activity of ni in alkaline media through oxygen-vacancy-rich CeO_2/Ni heterostructures, Angew. Chem. Int. Ed. 58 (40) (2019) 14179–14183.

[36] Y. Wu, J. Yang, M. Zheng, D. Hu, T. Salim, B. Tang, Z. Liu, S. Li, Two-dimensional cobalt ferrite through direct chemical vapor deposition for efficient oxygen evolution reaction, Chin. J. Catal. 55 (2023) 265–277.

[37] T. Guo, L. Li, Z. Wang, Recent development and future perspectives of amorphous transition metal-based electrocatalysts for oxygen evolution reaction, Adv. Energy Mater. 12 (24) (2022) 2200827.

[38] R. Elakkiya, G. Maduraiveeran, Two-dimensional earth-abundant transition metal oxides nanomaterials: synthesis and application in electrochemical oxygen evolution reaction, Langmuir 36 (17) (2020) 4728–4736.

[39] F. Song, L. Bai, A. Moysiadou, S. Lee, C. Hu, L. Liardet, X. Hu, Transition metal oxides as electrocatalysts for the oxygen evolution reaction in alkaline solutions: an application-inspired renaissance, J. Am. Chem. Soc. 140 (25) (2018) 7748–7759.

[40] X. Xu, T. Wang, L. Dong, W. Lu, X. Miao, Energy-efficient hydrogen evolution reactions via hydrazine oxidation over facile synthesis of cobalt tetraoxide electrodes, ACS Sustain. Chem. Eng. 8 (21) (2020) 7973–7980.

[41] G.A. Gebreslase, M.V. Martínez-Huerta, M.J. Lázaro, Recent progress on bimetallic NiCo and CoFe based electrocatalysts for alkaline oxygen evolution reaction: a review, J. Energy Chem. 67 (2022) 101–137.

[42] A. Tahir, F. Arshad, T. Haq, I. Hussain, S.Z. Hussain, H. Rehman, Roles of metal oxide nanostructure-based substrates in sustainable electrochemical water splitting: recent development and future perspective, ACS Appl. Nano Mater. 6 (3) (2023) 1631–1647.

[43] S. Zhang, X. Wei, S. Dai, H. Wang, M. Huang, Efficient hydrazine electro-oxidation achieved by tailored electron injection into Fe (III) sites activating dehydrogenation, Adv. Funct. Mater. 34 (10) (2023) 2311370.

[44] J. Hao, K. Wu, C. Lyu, Y. Yang, H. Wu, J. Liu, N. Liu, W.-M. Lau, J. Zheng, Recent advances in interface engineering of Fe/Co/Ni-based heterostructure electrocatalysts for water splitting, Mater. Horiz. 10 (7) (2023) 2312–2342.

[45] Q. Wu, A. Dong, C. Yang, L. Ye, L. Zhao, Q. Jiang, Metal-organic framework derived Co_3O_4@Mo-Co_3S_4-Ni_3S_2 heterostructure supported on Ni foam for overall water splitting, Chem. Eng. J. 413 (2021) 127482.

[46] F. Barati, M. Grossnickle, S. Su, R.K. Lake, V. Aji, N.M. Gabor, Hot carrier-enhanced interlayer electron–hole pair multiplication in 2D semiconductor heterostructure photocells, Nat. Nanotechnol. 12 (12) (2017) 1134–1139.

[47] F. Hu, M. Kim, Y. Zhang, Y. Luan, K.M. Ho, Y. Shi, C.Z. Wang, X. Wang, Z. Fei, Tailored plasmons in pentacene/graphene heterostructures with interlayer electron transfer, Nano Lett. 19 (9) (2019) 6058–6064.

[48] V. Mishra, A. Praveen, D. Raveendran, A. Chandrasekar, V. Mahalingam, Co_9S_8/$CoTe_2$ n-n type heterojunction: a heterogenic interfacial integration of Co_9S_8 and $CoTe_2$ phases for energy-efficient hydrazine oxidation assisted hydrogen production, Small 21 (10) (2025) 2412372.

[49] F. Liu, Q. Liang, Z. Li, M. Liu, N. Yue, Z. Wang, X. Zou, W. Zhang, Hierarchical FeO_xH_y@Ni_3B hybrid for efficient alkaline oxygen evolution at high current density, J. Energy Chem. 94 (2024) 599–607.

[50] F. Xie, A kinetic control strategy for one-pot synthesis of efficient bimetallic metal-organic framework/layered double hydroxide heterojunction oxygen evolution electrocatalysts, Adv. Funct. Mater. 33 (13) (2023) 2211260.

[51] H.-M. Yang, H.-Y. Wang, M.-L. Sun, Z.-Y. Yuan, Interface engineering of bifunctional nickel hydroxide/ nickel phosphide heterostructure for efficient intermittent hydrazine-assisted water splitting, Chem. Eng. J. 475 (2023) 146134.

[52] Y. Wu, S. Ji, H. Wang, B. Pollet, X. Wang, R. Wang, A highly efficient water electrolyser cell assembled by asymmetric array electrodes based on Co, Fe-doped $Ni(OH)_2$ nanosheets, Appl. Surf. Sci. 528 (2020) 146972.

[53] B. Li, L.-Y. Dai, W.-S. Wang, H.-Y. Xu, Urchin-like Co_3O_4 as a heterogeneous peroxymonosulfate catalyst for crystal violet degradation: reaction kinetics and process optimization, Mater. Today Commun. 33 (2022) 104388.

[54] G. Kresse, J. Hafner, Ab initio molecular dynamics for liquid metals, Phys. Rev. B 47 (1) (1993) 558–561.

[55] G. Kresse, J. Hafner, Ab initio molecular-dynamics simulation of the liquid-metal–amorphous-semiconductor transition in germanium, Phys. Rev. B 49 (20) (1994) 14251–14269.

[56] G. Kresse, J. Furthmüller, Efficiency of ab initio total energy calculations for metals and semiconductors using a plane-wave basis set, Comput. Mater. Sci. 6 (1) (1996) 15–50.

[57] J.P. Perdew, K. Burke, M. Ernzerhof, Generalized gradient approximation made simple, Phys. Rev. Lett. 77 (18) (1996) 3865–3868.

[58] G. Kresse, D. Joubert, From ultrasoft pseudopotentials to the projector augmented-wave method, Phys. Rev. B 59 (3) (1999) 1758–1775.

[59] S.L. Dudarev, G.A. Botton, S.Y. Savrasov, C.J. Humphreys, A.P. Sutton, Electron-energy-loss spectra and the structural stability of nickel oxide: an LSDA+U study, Phys. Rev. B 57 (3) (1998) 1505–1509.

[60] Z. Huang, F. Han, M. Li, Z. Zhou, X. Guan, L. Guo, Which phase of iron oxyhydroxides (FeOOH) is more competent in overall water splitting as a photocatalyst, goethite, akaganeite or lepidocrocite? A DFT-based investigation, Comput. Mater. Sci. 169 (2019) 109110.

[61] V. Singh, M. Kosa, K. Majhi, D.T. Major, Putting DFT to the test: a first-principles study of electronic, magnetic, and optical properties of Co_3O_4, J. Chem. Theory Comput. 11 (1) (2015) 64–72.

[62] S. Grimme, J. Antony, S. Ehrlich, H. Krieg, A consistent and accurate ab initio parametrization of density functional dispersion correction (DFT-D) for the 94 elements H–Pu, J. Chem. Phys. 132 (15) (2010) 154104.

[63] S. Grimme, S. Ehrlich, L. Goerigk, Effect of the damping function in dispersion corrected density functional theory, J. Comput. Chem. 32 (7) (2011) 1456–1465.

[64] K. Momma, F. Izumi, VESTA 3 for three-dimensional visualization of crystal, volumetric and morphology data, J. Appl. Cryst. 44 (2011) 1272–1276.

[65] Y. Hinuma, Y. Kumagai, I. Tanaka, F. Oba, Effects of composition, crystal structure, and surface orientation on band alignment of divalent metal oxides: a first-principles study, Phys. Rev. Mater. 2 (12) (2018) 124603.

[66] Y. Hinuma, Y. Kumagai, F. Oba, I. Tanaka, Categorization of surface polarity from a crystallographic approach, Comput. Mater. Sci. 113 (2016) 221–230.

[67] A. Togo, I. Tanaka, First principles phonon calculations in materials science, Scr. Mater. 108 (2015) 1–5.

[68] S. Takamoto, C. Shinagawa, D. Motoki, K. Nakago, W. Li, I. Kurata, T. Watanabe, Y. Yayama, H. Iriguchi, Y. Asano, T. Onodera, T. Ishii, T. Kudo, H. Ono, R. Sawada, R. Ishitani, M. Ong, T. Yamaguchi, T. Kataoka, A. Hayashi, N. Charoenphakdee, T. Ibuka, Towards universal neural network potential for material discovery applicable to arbitrary combination of 45 elements, Nat. Commun. 13 (1) (2022) 2991.

[69] S. Takamoto, D. Okanohara, Q.J. Li, J. Li, Towards universal neural network interatomic potential, J. Materiomics 9 (3) (2023) 447–454.

[70] D.R.S. Saputro, P. Widyaningsih, Limited memory Broyden–Fletcher–Goldfarb–Shanno (L-BFGS) method for parameter estimation on geographically weighted ordinal logistic regression (GWOLR), AIP Conf. Proc. 1868 (1) (2017) 040009.

[71] R.F.W. Bader, Atoms in molecules, Acc. Chem. Res. 18 (1) (1985) 9–15.

[72] W. Tang, E. Sanville, G. Henkelman, A grid-based Bader analysis algorithm without lattice bias, J. Phys. Condens. Matter 21 (8) (2009) 084204.

[73] M. Yu, D.R. Trinkle, Accurate and efficient algorithm for Bader charge integration, J. Chem. Phys. 134 (6) (2011) 064111.

[74] E. Sanville, S.D. Kenny, R. Smith, G. Henkelman, Improved grid-based algorithm for Bader charge allocation, J. Comput. Chem. 28 (5) (2007) 899–908.

[75] S. Jiao, L. Xu, K. Hu, J. Li, S. Gao, D. Xu, Morphological control of α-FeOOH nanostructures by electrodeposition, J. Phys. Chem. C 114 (1) (2010) 269–273.

[76] S. Farhadi, Z. Heydari-Chegeni, M. Mousavi, Facile template-free hydrothermal synthesis of Co_3O_4 hollow microspheres constructed by nanoparticles using $[Co(NH_3)_4CO_3]NO_3$ and their photocatalytic activity, J. Alloy. Compd. 692 (2017) 923–933.

[77] D.D.M. Prabaharan, K. Sadaiyandi, M. Mahendran, S. Sagadevan, Precipitation method and characterization of cobalt oxide nanoparticles, Appl. Phys. A 123 (4) (2017) 264.

[78] K. Arathi, K.L. Nagashree, M.P. Rao, K. Raj, P. Shivakumar, D.H. Nagaraju, CuO/Co_3O_4 heterojunctions for catalytic nitroarenes reduction and oxygen evolution reaction, Inorg. Chem. Commun. 169 (2024) 113106.

[79] F. Nur Indah Sari, S. Abdillah, J.-M. Ting, FeOOH-containing hydrated layered iron vanadate electrocatalyst for superior oxygen evolution reaction and efficient water splitting, Chem. Eng. J. 416 (2021) 129165.

[80] B. Zhang, L. Wang, Z. Yajun, Y. Ding, Y. Bi, Ultrathin FeOOH nanolayers with abundant oxygen vacancies on $BiVO_4$ photoanodes for efficient water oxidation, Angew. Chem. Int. Ed. 57 (8) (2018) 2248.

[81] J. Hu, S. Li, J. Chu, S. Niu, J. Wang, Y. Du, Z. Li, X. Han, P. Xu, Understanding the phase-induced electrocatalytic oxygen evolution reaction activity on FeOOH nanostructures, ACS Catal. 9 (12) (2019) 10705–10711.

[82] P. Mannu, D. Kumar, N. Ta Thi Thuy, A. Mariappan, Y.C. Shao, H. Ishii, Y.-C. Huang, A. Kandasami, T. Oh, W.C. Chou, C.-L. Chen, J.-L. Chen, C.L. Dong, Tuning of oxygen vacancies in Co_3O_4 electrocatalyst for effectiveness in urea oxidation and water splitting, Small 21 (4) (2024) 2403744.

[83] D. Yin, D. Chen, Y. Zhang, W. Wang, Q. Quan, W. Wang, Y. Meng, Z. Lai, Z. Yang, S. P. Yip, C.-Y. Wong, B. Xiuming, X. Wang, J. Ho, Synergistic active phases of transition metal oxide heterostructures for highly efficient ammonia electrosynthesis, Adv. Funct. Mater. 33 (50) (2023) 2303803.

[84] X. Wang, X. Wang, J. Huang, S. Li, A. Meng, Z. Li, Interfacial chemical bond and internal electric field modulated Z-scheme Sv-$ZnIn_2S_4$/$MoSe_2$ photocatalyst for efficient hydrogen evolution, Nat. Commun. 12 (1) (2021) 4112.

[85] C. Tang, R. Zhang, W. Lu, Z. Wang, D. Liu, S. Hao, G. Du, A.M. Asiri, X. Sun, Energy-saving electrolytic hydrogen generation: Ni_2P nanoarray as a high-performance non-noble-metal electrocatalyst, Angew. Chem. Int. Ed. 56 (3) (2016) 842–846.

[86] C. Guo, L. Zhang, J. Miao, J. Zhang, C. Li, DNA-functionalized graphene to guide growth of highly active Pd nanocrystals as efficient electrocatalyst for direct formic acid fuel cells, Adv. Energy Mater. 3 (2) (2013) 167–171.

[87] T. Yu, G. Liu, T. Nie, Z. Wu, Z. Song, S. Xiaoliang, Y.-F. Song, Pt-loaded CoFe-Layered double Hydroxides for simultaneously driving HER and HzOR, ACS Catal. 14 (2024) 14937–14946.

[88] R. Govindasamy, C.J. Moon, R.A. Senthil, V. Maheskumar, A. Kumar, S. Lee, M. Ubaidullah, M.Y. Choi, Ultra-low voltage hydrazine splitting with pulsed laser harnessed Ir/CoP for efficient Zn-hydrazine battery systems, Chem. Eng. J. 522 (2025) 167074.

[89] E. Allahyari, G. Barati Darband, A. Davoodi, Pulsed-potential electrodeposition of Ni-Mn-P@Co-S: study of pulse parameters on electrocatalytic activity for hydrogen and oxygen evolution reactions, Fuel 405 (2026) 136678.

[90] W. Pan, J. Yuan, P. Wang, J. Wang, Y. Zhao, G. Wang, H. Yu, Z. Wen, Efficient ultra-low voltage electrolysis of CO_2 coupling with hydrazine oxidation degradation, Appl. Catal. B: Environ. Energy 351 (2024) 124011.

[91] X. He, Z. Li, J. Yao, K. Dong, X. Li, L. Hu, S. Sun, Z. Cai, D. Zheng, Y. Luo, B. Ying, M.S. Hamdy, L. Xie, Q. Liu, X. Sun, High-efficiency electrocatalytic nitrite reduction toward ammonia synthesis on CoP@TiO_2 nanoribbon array, Science 26 (7) (2023) 107100.

[92] L.-Y. Dai, B. Li, H.-Y. Xu, W.-S. Wang, S.-Q. Zhang, Y. Xu, S.-Y. Qi, X.-L. He, L.-G. Jin, Magnetic nanoreactor Fe_3O_4@HNTs as heterogeneous Fenton-like catalyst for acid fuchsin degradation: efficiency, kinetics and mechanism, J. Phys. Chem. Solid 180 (2023) 111445.